New Supply-Air Solar Wall with Thermal Storage Designed to Preheat Fresh Air: Development of a Numerical Model Adapted to Building Energy Simulation

Rima Abou Ibrahim, Pierre Tittelein, Stéphane Lassue, Fadi Hage Chehade, Laurent Zalewski

▶ **To cite this version:**

Rima Abou Ibrahim, Pierre Tittelein, Stéphane Lassue, Fadi Hage Chehade, Laurent Zalewski. New Supply-Air Solar Wall with Thermal Storage Designed to Preheat Fresh Air: Development of a Numerical Model Adapted to Building Energy Simulation. Applied Sciences, 2022, 12 (8), pp.3986. ⟨10.3390/app12083986⟩. ⟨hal-03714492⟩

HAL Id: hal-03714492

https://hal.science/hal-03714492v1

Submitted on 5 Jul 2022

HAL is a multi-disciplinary open access archive for the deposit and dissemination of scientific research documents, whether they are published or not. The documents may come from teaching and research institutions in France or abroad, or from public or private research centers.

L'archive ouverte pluridisciplinaire **HAL**, est destinée au dépôt et à la diffusion de documents scientifiques de niveau recherche, publiés ou non, émanant des établissements d'enseignement et de recherche français ou étrangers, des laboratoires publics ou privés.

HAL Authorization

applied sciences

MDPI

Article

New Supply-Air Solar Wall with Thermal Storage Designed to Preheat Fresh Air: Development of a Numerical Model Adapted to Building Energy Simulation

Rima Abou Ibrahim [1], Pierre Tittelein [1], Stéphane Lassue [1], Fadi Hage Chehade [2] and Laurent Zalewski [1,*]

[1] Univ. Artois, IMT Nord Europe, Junia, Univ. Lille, ULR 4515, Laboratoire de Génie Civil et Géo-Environnement—LGCgE, F-62400 Béthune, France; rima_abouibrahim@ens.univ-artois.fr (R.A.I.); pierre.tittelein@univ-artois.fr (P.T.); stephane.lassue@univ-artois.fr (S.L.)

[2] Modeling Center, Doctoral School of Science and Technology, Lebanese University, Hadath 99000, Lebanon; fchehade@ul.edu.lb

* Correspondence: laurent.zalewski@univ-artois.fr

Abstract: Façades built with integrated passive solar systems hold great promise for improving the energy performance of buildings and achieving indoor comfort conditions. Among these techniques, solar air preheating systems with different configurations have proven their ability to reduce the energy consumption of buildings during the heating season. In this study, we propose a ventilated solar wall (VSW) with a thermal storage unit intended for preheating ventilation air. The final aim of this study is to determine the thermal performance of the studied VSW over a significant time period (during the heating season) under various climatic conditions when it is integrated into the building envelope. Therefore, for this purpose, a simplified model was developed to be coupled to a building energy simulation (BES) code. The results from the detailed steady-state 2D computational fluid dynamics (CFD) model show that the thermal efficiency of the VSW ranged from 55% to 70% as the air mass flow rate increased from 0.008 kg/s to 0.02 kg/s for a surface of 2.15 m^2. These results were used to evaluate the convective heat transfer coefficients in the two air cavities and to validate the simplified model. The results indicate good agreement between the two models.

Keywords: building's passive heating; ventilated façades; supply-air system; CFD; low-tech

check for updates

Citation: Ibrahim, R.A.; Tittelein, P.; Lassue, S.; Chehade, F.H.; Zalewski, L. New Supply-Air Solar Wall with Thermal Storage Designed to Preheat Fresh Air: Development of a Numerical Model Adapted to Building Energy Simulation. *Appl. Sci.* **2022**, *12*, 3986. https://doi.org/10.3390/app12083986

Academic Editor: Cesare Biserni

Received: 10 March 2022
Accepted: 6 April 2022
Published: 14 April 2022

Publisher's Note: MDPI stays neutral with regard to jurisdictional claims in published maps and institutional affiliations.

Copyright: © 2022 by the authors. Licensee MDPI, Basel, Switzerland. This article is an open access article distributed under the terms and conditions of the Creative Commons Attribution (CC BY) license (https://creativecommons.org/licenses/by/4.0/).

1. Introduction

Passive solar façades with their primary modes of operation (Figure 1), namely, exhaust [1–3], supply [4–7], indoor air curtain [8–10], and outdoor air curtain, have proven their ability to contribute toward improving the thermal efficiency of buildings when they are integrated into their envelope (Table 1).

Supply-air façades are low-tech devices that can recuperate a part of the heat losses from the inside and capture solar gains to primarily heat the fresh air blown inside, thus reducing the heating load of buildings during the heating season. The studied systems can be classified into different groups according to several criteria: transparent or opaque façades, mechanically or naturally ventilated façades, façades with one or two layers of airflow, and façades with or without thermal storage.

Supply-air windows are a variation of multiple-pane windows in which air is drawn in from the outside and heated within the cavity by convection, conduction, and radiation [11]. Carlos et al. [4] studied experimentally the thermal performance of a naturally ventilated double window with one airflow layer during the heating season. This study was carried out in a test cell in a mountainous region in central Portugal exposed to real outdoor weather conditions. It was discovered that such window systems act as efficient heat exchangers using transmission heat losses and solar radiation to preheat the ventilated air, thereby reducing domestic energy consumption. A triple-glazed supply-air window

(Paziaud window) was investigated numerically by Gloriant et al. [5]. Laminar forced convection was considered for the airflow in the air gaps. The authors developed models which can be implemented in building simulation codes by referring to the results obtained with the CFD code. The energy efficiency of this system was demonstrated by the calculated performance indicators.

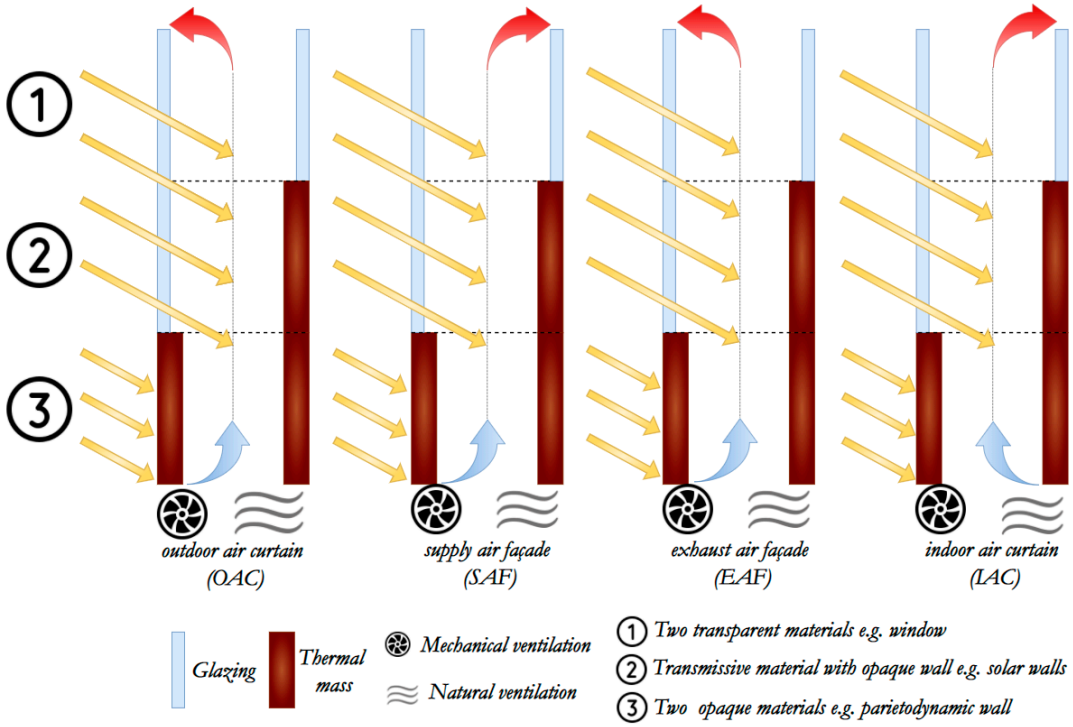

Figure 1. Solar façade types (inspired by [12–15]).

Similar research was reported by Michaux et al. [6]. The authors evaluated the energy performance of an airflow window via a numerical simulation and an experimental test. The air supply preheating was found to be significant, ranging from approximately 10–20 °C without solar radiation and during sunny periods, respectively. Kaboré et al. [7] presented an airflow window equipped with heated glazing. The results indicated that heated air-circulation windows help reduce heating energy consumption compared to traditional double-glazed windows. Heated airflow windows can replace the conventional electric heating solutions.

Another type of these envelopes is the double-skin façade (DSF). Two layers of glass and an air cavity between them (that can be equipped with Venetian blinds) constitute the DSF [16]. The DSF studied by Faggembauu et al. [17] was made up of a single outer glass layer, an air channel, and an inner layer comprising two zones: a double-glazed area at the top and an insulated panel at the base. The behavior of the ventilated façade was studied over one year under Mediterranean climatic conditions. As a result, it was proven that a well-designed façade can reduce indoor gains in summer and use enthalpy gains to reduce energy consumption in winter. From the perspective of energy demand for cooling and heating, a numerical and experimental analysis of naturally ventilated DSF with Venetian blinds showed good application in the Yangtze River area in China [16]. Fallahi et al. [18] evaluated a double-skin façade with a thermal mass. Three different configurations were proposed: replacement of the aluminum shading device between the two panes, and replacement of the interior or the exterior pane of the classic DSF by a concrete thermal mass. The results indicated that this concept of mechanically ventilated DSF can, based on the configuration, save from 21% to 26% of energy in summer and from 41% to 59% in winter compared to conventional DSFs without a thermal mass.

Table 1. Characteristics of a selection of solar wall configurations.

Type of Solar Wall	References	Operating Mode	Operating Condition	Approach	Ventilated Air Cavity Thickness	Thermal Performance
SAF *(Double-skin façade)*	*Khosravi and A. Mahdavi* [11]	natural convection	steady	numerical	50 mm	A = 80 to 85%
IAC *(Trombe wall)*	*Leang* et al. [20]	natural convection	dynamic	numerical	45 mm	C = 20 to 30%
SAF *(Parietodynamic window)*	*Michaux* et al. [21]	forced convection	dynamic	merical	15 mm	C = 28 to 46%
SAF *(Parietodynamic wall)*	*Fantucci* et al. [13]	forced convection	steady	experimental	50 mm	A = 9 to 20%
IAC *(Trombe wall)*	*Hong* et al. [22]	natural convection	steady	numerical	80 to 180 mm	B = 27.72 to 32.6%
IAC *(Trombe wall)*	*Bojić* et al. [23]	natural convection	dynamic	numerical	100 mm	C = 20%
IAC *(Trombe wall)*	*Jaber and Ajib* [24]	natural convection	dynamic	numerical	150 mm	C = 20.9 to 32.5%
SAF *(Solar dynamic buffer zone)*	*Richman and Pressnail* [19]	forced convection	steady	experimental	93 mm	B = 25 to 30%
SAF *(Solar dynamic buffer zone)*	*Richman and Pressnail* [25]	forced convection	dynamic	numerical	93 mm	C = 35%

Fantucci et al. [13] investigated experimentally two configurations of a ventilated opaque double-skin façade (parietodynamic wall) based on hollow clay bricks. The laboratory tests for the supply-air façade configuration showed that, depending on the airflow rate, a preheating efficiency of 9 to 20% can be achieved. The heat loss reduction for the exhaust-air façade configuration was measured as being between 43 and 68%.

Richman and Pressnail [19] investigated through experiments and numerical simulations the performance of a solar dynamic buffer zone (SDBZ) within a curtain wall system. This SDBZ is a façade system capable of collecting heat from outside. The authors found that the SDBZ developed a thermal efficiency of 25 to 30%, placing this system in the medium range for solar air collectors.

- Performance indicators

Many indicator definitions can be used to evaluate the thermal performance of ventilated solar façades under different operating configurations.

$$\text{A}: \ \eta_A = \frac{T_{out} - T_{ext}}{T_{in} - T_{ext}} \tag{1}$$

$$\text{B}: \ \eta_B = \frac{Q_u}{AI} \tag{2}$$

where $Q_u(W)$, the useful heat gain, is given by the following equation:

$$Q_u = \dot{m} C_p (T_{out} - T_{in}) \tag{3}$$

where $\dot{m}$ ($\text{kg}\cdot\text{s}^{-1}$) is the mass flow rate, C_p ($\text{J}\cdot\text{kg}^{-1}\cdot\text{K}^{-1}$) is the specific heat capacity of the air, and $T_{out}(^{\circ}\text{C})$. and $T_{in}(^{\circ}\text{C})$. are, respectively, the air temperature at the outlet and the

inlet of the VSW. Moreover, I is the irradiance ($W \cdot m^{-2}$) and $A(m^2)$ is the surface area of the VSW.

C: Heating load savings

Reduction in heating energy consumption after the integration of the passive solar system into the building envelope.

In this paper, we study a new configuration of a supply-air façade with a storage element used to preheat fresh air for winter ventilation. Two parallel panes of glass are placed in front of the exterior wall of a building in such a way as to form two air gaps. The exterior concrete wall serves as a thermal mass that can store thermal energy in the form of sensible heat. This configuration of the opaque parietodynamic solar façade makes it possible to lengthen the path traveled by the air. To our knowledge, this system has not been studied in the literature.

To assess the complex airflow in the two cavities of the VSW, detailed numerical modeling that represents the heat, mass, and momentum transfer is needed. This type of numerical modelling can be obtained with the CFD tool, with which the detailed temperature and velocity distributions for each position in the cavities are calculated with a high degree of accuracy by solving the conservation equations for mass, momentum, and thermal energy when boundary conditions are properly specified [26]. This approach has proven its effectiveness in modeling the various heat transfer modes that are presented in such a system [5,6]. It is also a more flexible and less expensive tool compared to physical experiments because it enables unlimited repeatability for remodeling and simulation [27]. We supposed that it would be reasonable to start with numerical simulations in this first phase of researching a unique and innovative solar wall since they allow for evaluating a wide range of different designs at a low cost. Hence, for this study, CFD was chosen as the investigation tool to examine the performance of the ventilated solar wall. However, an experimental validation will be carried out at a later time in order to provide significant added value to the numerical investigations.

On the other hand, the solar wall model to be developed must assess the impact of this passive solar system on the energy behavior of a building over a long period of time while considering its interaction with the exterior and interior environments. The multizone approach is the method used by the majority of dynamic thermal simulation software programs for buildings, TRNSYS, EnergyPlus, ESP-r, and so on. This simple approach is based on the main assumption that each zone of the building, when assimilated to a node, is a homogeneous volume characterized by uniform state variables. In general, a node can represent a wall, a room, or even a set of rooms. A heat balancing process is carried out for each of the zones. Thus, the model dedicated to the energy simulation of the solar wall over a long period of time requires a relatively short calculation time.

Thus, CFD models do not allow for the calculation of the dynamic regime over long periods of time (annually) with reasonable computing resources [28]. CFD simulation is a popular and effective method for steady-state performance analysis. Consequently, a fast and reliable numerical model that can be integrated into energy simulation tools is required for dynamic annual energy analysis.

This paper is structured as follows. Section 2 describes the ventilated solar façade from this study. Section 3 provides detailed data about the mathematical (CFD) model of the ventilated solar wall, as well as an analysis and discussions to address the performance of the VSW under steady-state conditions. Section 4 describes the developed simplified model adapted to building simulation, and Section 5 contains the main research findings of this study.

2. System Description

A vertical section (2D) of the ventilated solar wall studied numerically is shown in Figure 2. This comprises (from outside to inside) an outer glazing in contact with the exterior environment, an outer air gap, a second glazing with a low-emissivity coating on the outer side, an inner air gap, a massive wall, and insulation. The two air gaps form a

U-shaped channel. Fresh air enters the southern-facing solar wall through the inlet opening located at the top of the outer pane at a temperature equal to that of the outdoor air. It flows down into the first air gap delimited by the two glazings and then flows upward into the second air gap delimited by the glazing and the storage wall. The solar energy absorbed by the two panes and mainly by the concrete massive wall is transferred to the fresh air passing through the ventilated cavities. The air is also preheated by recovering part of the heat loss from the interior. The thermal energy stored in the form of sensible heat in the concrete massive wall is used to meet energy needs at night or during cloudy daytime periods. Preheated air enters the building through the outlet opening at the top of the opaque layer with an unknown temperature. The flow of air at a low speed in the solar wall is induced by the depressurization of interior spaces by mechanical means. The glazing with a low-e coating prevents heat from re-radiating to the outside, thus improving the performance of the VSW by taking advantage of the greenhouse effect during the day and reducing losses to the outside at night. A black heat-absorbing material is installed on the exterior surface of the massive wall to maximize the solar energy absorbed by the latter. Both the upper and the lower horizontal surfaces of the VSW are treated as adiabatic.

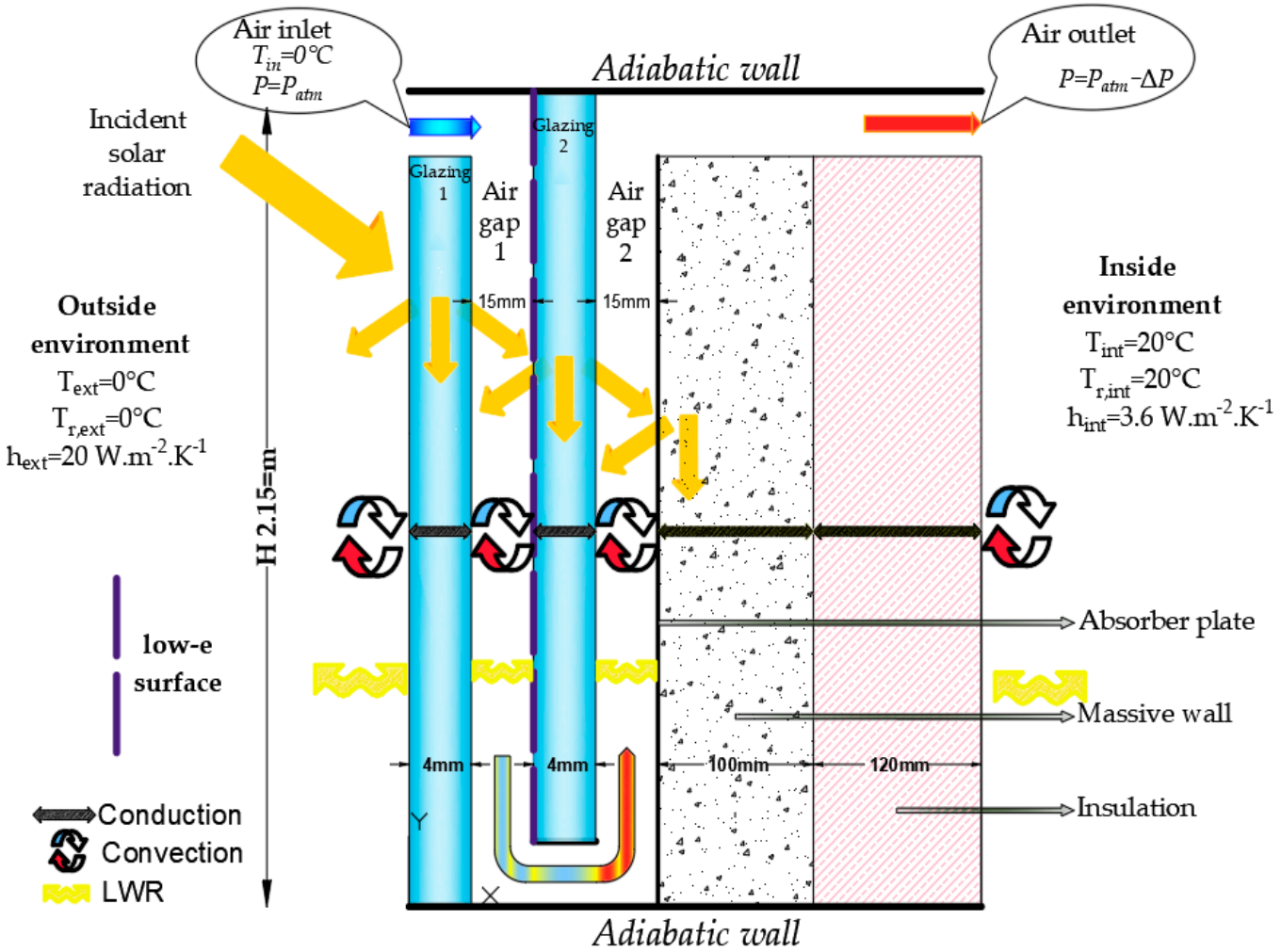

Figure 2. The physical model of the VSW (*not to scale*).

Figure 2 shows the different heat transfer mechanisms involved in the model: thermal conduction within each solid layer, convection, long-wave radiation (LWR) in the two air gaps as well as in the surrounding environments of the VSW, and solar radiation absorption. The thermophysical properties of the outer and inner glass panes as well as the opaque layers of the VSW are given in Tables 2 and 3 respectively.

Table 2. Assumed properties of the outer and inner glass panes.

	Symbol	Outer Glass Pane (4 mm)	Inner Glass Pane (4 mm)
Thickness (mm)	e	4	4
Absorbance (-)	α	0.015	0.156
Reflectance (-)	ϱ	0.079	0.11
Transmittance (-)	τ	0.906	0.734
Emissivity (-)	ε	0.84/0.84	0.17/0.84
Density ($kg \cdot m^{-3}$)	ρ	2500	2500
Specific heat capacity ($J \cdot kg^{-1} \cdot K^{-1}$)	C_p	840	840
Thermal conductivity ($W \cdot m^{-1} \cdot K^{-1}$)	λ	1	1

Table 3. Thermophysical properties of the opaque layers of the VSW.

	Symbol	Massive Wall (Concrete)	Insulation
Thickness (mm)	e	100	120
Absorbance (-)	α	0.9	0.9
Emissivity (-)	ε	0.9	0.9
Density ($kg \cdot m^{-3}$)	ρ	1900	30
Specific heat capacity ($J \cdot kg^{-1} \cdot K^{-1}$)	C_p	949	880
Thermal conductivity ($W \cdot m^{-1} \cdot K^{-1}$)	λ	0.82	0.041

- Properties of materials
- Absorption of solar radiation in the two glazings and the massive wall considering multiple reflections

When the incident solar radiation (direct and diffuse radiation) reaches the external surface of the first glazing, it is partly absorbed by the latter and partly transmitted to the second glazing, and the remaining part is reflected back to the outside environment. Likewise, the part which reaches the second glazing is divided into reflected, absorbed, and transmitted radiation to the massive wall. The fraction which is transferred to the massive wall is then absorbed or reflected by it. The part reflected towards the first glazing is again reflected, absorbed, or transmitted by it.

The determination of the absorbed heat at each layer of the VSW is relatively complicated due to the multi-reflection between them. The solar energy absorption factors for the two panes as well as the massive wall, which depend on the optical characteristics of the panes as well as the absorption factor of the storage wall, were calculated:

$$\xi_{v1} = \alpha_{v1} + \frac{\alpha_{v1}(1-\alpha_m)\tau_{v1}}{1-\varrho_{v1}(1-\alpha_m)} \quad (4)$$

$$\xi_{v2} = \frac{\tau_1\alpha_2}{1-\varrho_2\varrho_1} + \frac{\tau_1\tau_2\varrho_m\alpha_2}{1-\varrho_m\varrho_2}\left(1+\frac{\varrho_2\varrho_1}{1-\varrho_2\varrho_1}\right) \quad (5)$$

$$\xi_m = \alpha_m\tau_1\tau_2\left(1+\frac{\varrho_1(\varrho_2+\tau_2\varrho_m)}{1-\varrho_1\varrho_2} + \frac{\varrho_m\varrho_2}{1-\varrho_m\varrho_2}\right) \quad (6)$$

The results obtained from these relations were compared with the absorption coefficients calculated with the WINDOW 7 software [29], that is based on an exact analytical calculation. Errors were estimated at less than 4.5% (Table 4).

Table 4. Comparison between the values of the solar radiation absorption coefficients for the two glazings and the solar wall calculated by the correlations and those obtained with the WINDOW software.

	ξ_{v1}	ξ_{v2}	ξ_m
Correlations	0.0164	0.1532	0.6139
WINDOW 7	0.017	0.1468	0.6171
Error (%)	3.71	4.38	0.43

3. Mathematical (CFD) Model of the Ventilated Solar Wall

Computational fluid dynamics, which is based on the solution of a standard set of conservation equations, can accurately describe the flow regime, velocity, and temperature of the airflow in the cavity, as well as determine the heat transfer coefficients in the given system. The main advantage of this method is its ability to collect very accurate information on thermofluidic behaviors in walls and cavities; however, this leads to a significantly long time being required to complete the calculation. This implies that such a method is only appropriate for studying transient state phenomena under steady-state conditions or when they are of relatively short duration, not for studying transient states [30].

With CFD modeling, the geometric domain of the VSW is divided into many cells. The three conservation equations of mass, momentum, and energy are solved for each cell to predict the field variables (temperature and velocity). Ansys Fluent code was used for this CFD study to investigate the fluid flow and heat transfer characteristics in the ventilated cavities of the solar wall described in the previous section. The partial differential equations were then numerically solved using the finite volume method.

A two-dimensional steady-state laminar (Re < 2300) flow was assumed. A pressure-based double-precision solver was selected to solve the set of equations used. The discrete-ordinates (DO) radiation model was employed to solve the radiative transfer equation (RTE). Solar radiation was modeled as internal heat gains added to both glass panes, and for the massive wall it was modeled as surface heat generation at its external surface using the solar energy absorption factors determined previously (Section 2). Simulations considering and not considering the gravity force were performed. At first, simulations not considering the gravity force were performed, as this reduces the simulation time. However, after we noticed that gravity affected the velocity and temperature profiles and subsequently the convective heat transfer coefficients, we finally took it into account. Second-order upwind discretization schemes were imposed for pressure and momentum and first-order upwind for energy and DO. Convergence was reached when the scaled residuals reached values of 10^{-6} for the continuity, 10^{-8} for the velocity and DO intensity, and 10^{-7} for the energy. A uniform mass flow rate was imposed at the inlet of the geometry. The mass flow range was chosen in such a way as to achieve laminar flow.

Air entered within the VSW at an external (cold) temperature, T_{ext}, equal to 0 °C. On the internal (warm) side of the VSW, the temperature of the air, T_{int}, was fixed at 20 °C. The indoor and outdoor radiative temperatures had the same values as the indoor and outdoor air temperatures.

3.1. Governing Equations

The conservation equations for the fluid in the air cavities are written as:

- Mass conservation equation: Continuity equation

$$\frac{\partial \rho}{\partial t} + \nabla(\rho \vec{V}) = 0 \quad (7)$$

where $\vec{V} = u\,\vec{\mathrm{i}} + v\,\vec{\mathrm{j}}$ is the fluid velocity.

- Momentum conservation equation: Navier Stokes equation

This equation (derived from Newton's second law) states that the variation in a fluid cell's momentum is equal to the total of all forces acting on it.

$$\frac{\partial \vec{V}}{\partial t} + (\vec{V} \cdot \vec{grad})\vec{V} = -\frac{1}{\rho}\vec{grad}P + \nu\Delta\vec{V} + \vec{g} \quad (8)$$

- Energy conservation equation

According to the first law of thermodynamics, energy can be neither created nor destroyed.

$$\rho C_p(\vec{V} \cdot \vec{grad}T) = \lambda\Delta T \quad (9)$$

The air is considered a Newtonian fluid with thermophysical properties λ, ρ, μ, and C_p dependent on temperature (K), see Table 5.

Table 5. Thermophysical properties of the air as a function of its temperature (K).

	Polynomial Function
C_p (J·kg^{-1}·K^{-1})	$1064.957 - 0.40331\mathrm{T} + 0.000697\mathrm{T}^2$
λ (W·m^{-1}·K^{-1})	$0.0028586 + 7.822 \times 10^{-5}\mathrm{T}$
μ (kg·m^{-1}·s^{-1})	$-2.879045 \times 10^{-5} + 2.702918 \times 10^{-7}\mathrm{T} - 3.741942 \times 10^{-10}\mathrm{T}^2$
ρ (kg·m^{-3})	$2.363942 - 0.00399\mathrm{T}$

3.2. Boundary and Operating Conditions

- VSW entry

Air entered within the VSW at an external (cold) temperature, T_{ext}, equal to 0 °C. A mass flow rate was imposed.

$$T = T_{in} \text{ for } x = 0 \text{ mm and } 2135 \text{ mm} \leq y \leq 2150 \text{ mm} \quad (10)$$

- Internal surfaces of the two air gaps

A non-slip boundary condition was assigned for all solid walls; the surfaces of both the outer and the inner air channels were in contact with the fluid (air).

- Outer air channel:

$$u = v = 0 \text{ for } x = 4 \text{ mm and } 0 \text{ mm} \leq y \leq 2135 \text{ mm} \quad (11)$$

$$u = v = 0 \text{ for } x = 19 \text{ mm and } 15 \text{ mm} \leq y \leq 2150 \text{ mm} \quad (12)$$

- Inner air channel:

$$u = v = 0 \text{ for } x = 23 \text{ mm and } 15 \text{ mm} \leq y \leq 2150 \text{ mm} \quad (13)$$

$$u = v = 0 \text{ for } x = 38 \text{ mm and } 0 \text{ mm} \leq y \leq 2135 \text{ mm} \quad (14)$$

- Adiabatic regions

An adiabatic boundary condition was specified at the top and bottom sides of the VSW.

$$\frac{\partial T}{\partial y} = 0 \text{ for } y = 0 \text{ and } y = \mathrm{H} \quad (15)$$

- VSW outlet

A constant atmospheric pressure outlet condition was chosen for the simulation.

- Surface in contact with the external and internal ambients

At the external side of the glass pane in contact with the external environment and at the internal side of the insulation in contact with the internal environment, the values of

the external and internal heat transfer coefficients as well as the outdoor and indoor temperatures were chosen according to the ISO standard 15099 under winter conditions [31].

$$h_{ext} = 20\ \mathrm{W{\cdot}m^{-2}{\cdot}K^{-1}} \text{ and } T = T_{ext} = 0\ ^{\circ}\mathrm{C}\ in\ x = 0\ \mathrm{mm} \text{ and } 0\ \mathrm{mm} \leq y \leq 2135\ \mathrm{mm} \quad (16)$$

$$h_{int} = 3.60\ \mathrm{W{\cdot}m^{-2}{\cdot}K^{-1}} \text{ and } T = T_{in} = 20\ ^{\circ}\mathrm{C} in\ x = 258\ \mathrm{mm} \text{ and } 0\ \mathrm{mm} \leq y \leq 2135\ \mathrm{mm} \quad (17)$$

3.3. Grid Sensitivity Analysis

In this model, a structured mesh with a rectangular element was generated (see Figure 3). A finer mesh was applied near the surfaces of the two air cavities to achieve a higher resolution concerning the air movement in the cavities. Three simulation series were run, and a mesh sensitivity test was carried out to prove the mesh-independence of the numerical results. The total number of mesh elements was 282,366, including 125,184 cells for the air domain.

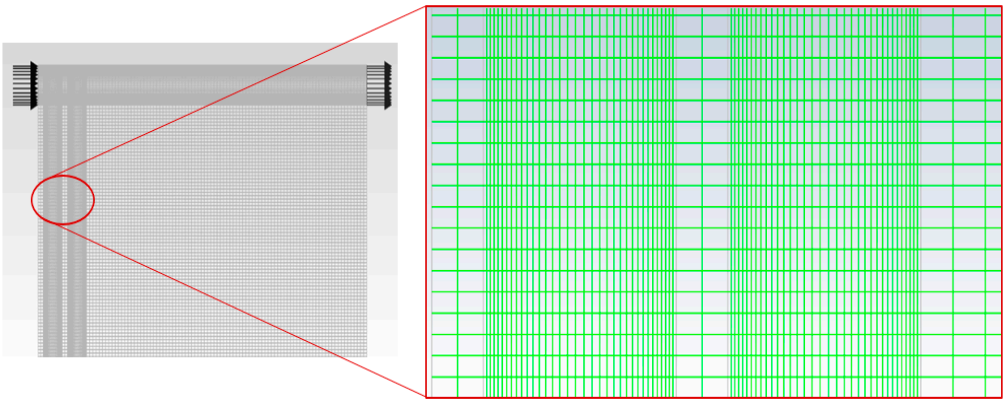

Figure 3. Detail of the mesh generated for the VSW.

3.4. Results

In this section, we represent the results obtained for an imposed airflow rate of 0.014 $\mathrm{kg{\cdot}s^{-1}}$ (40 $\mathrm{m^3{\cdot}h^{-1}}$) and an incident solar radiation of 300 $\mathrm{W{\cdot}m^{-2}}$.

The forced nature of the convective heat transfer regime was verified using the "buoyancy" ratio proposed by Padet et al. [32]:

$$RiRe = \frac{\rho g \beta (T_s - T_m) D_h^2}{\mu V} \quad (18)$$

Ri is the Richardson number.

The buoyancy forces are negligible if the buoyancy ratio is less than the critical value:

$$(RiRe)_c = 288 \quad (19)$$

The buoyancy ratio calculated for the set of simulations was below 100 for the two air gaps. The forced nature of the airflow was verified.

3.4.1. Temperature Profiles

- Outer Air Gap

At the inlet of the first outer air gap and the upper section of the VSW, the air temperature increased considerably. As air flowed downwards to the mid-section of the outer air gap, two parts in the air temperature profiles could be distinguished: the temperature rose next to the outer window and decreased near the inner window (Figure 4a).

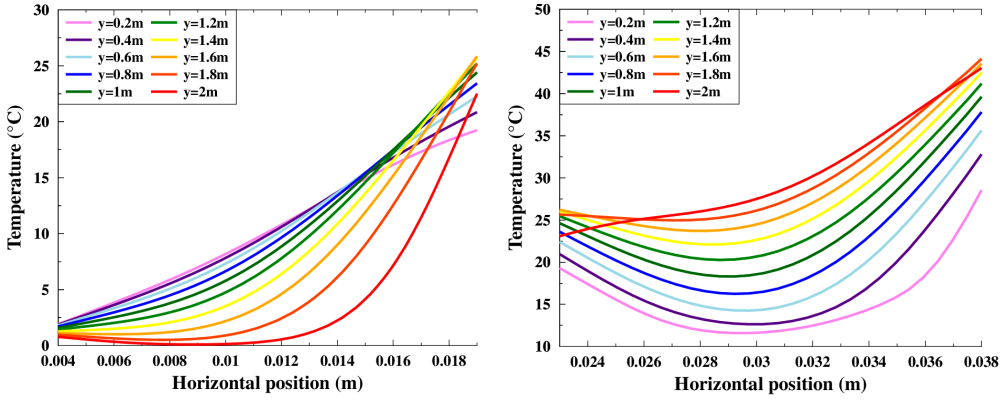

Figure 4. Variation in horizontal temperature profiles with VSW height: (**a**) outer air gap; (**b**) inner air gap.

- Inner Air Gap

As the air rose through the inner air gap, the temperature continuously increased until the air reached the top of the air gap (air outlet), where the air temperature began to decrease. This drop in temperature was due to heat exchange with the outer air gap, where the air temperature was close to the exterior temperature (Figure 4b).

The vertical distribution of air and channel surface temperatures is shown in Figure 5. We can see that, in the outer air gap, the bulk air temperature was higher than the temperature of the inner surface of the outer glazing. In the inner gap, the air bulk temperature was lower than the inner surface temperature of the second glazing for $y < 1.45$ m and higher than it for $y > 1.45$ m.

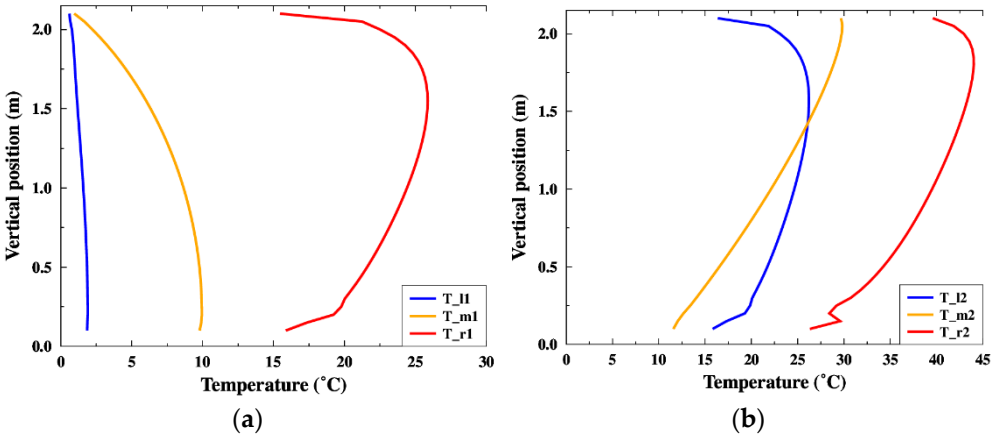

Figure 5. Temperature evolution of air and channel surfaces with VSW height: (**a**) outer air gap; (**b**) inner air gap. T_l and T_r represent the temperatures of the left and right surfaces of the air channel, respectively, and T_m represents the air bulk temperature.

Note that the air bulk temperature, T_m, is defined as:

$$T_m = \frac{1}{v_m S} \iint_S v(y) T(x,y) dx dy \tag{20}$$

where the mean velocity is defined as:

$$v_m = \frac{\int_0^e v(x) dx}{\int_0^e dx} \tag{21}$$

3.4.2. Convective Heat Transfer Coefficients

In Figure 6, we represent the local convective heat transfer coefficients calculated for the two surfaces of the internal and external air gap.

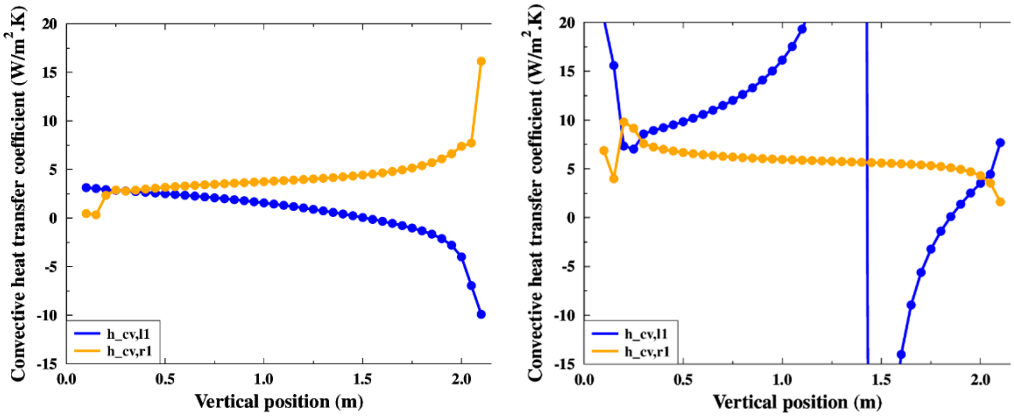

Figure 6. Local convective heat transfer coefficients in the (**a**) outer gap and (**b**) inner gap.

The convective heat exchange between the air cavity surface and the air is defined as:

$$q_{cv} = h_{cv}\,(T_s - T_f) \tag{22}$$

By definition, T_f is the temperature of the fluid sufficiently far from the surface, but since we are working in a parallel-plate vertical channel, T_f was calculated as the air bulk temperature (see Equation (20)). The bulk temperature was used for flows of internal forced convection, such as pipe flows and heat exchangers [33,34]. The local convection heat transfer coefficients h_{cv} between the air cavity surfaces and the airflow inside the channels were calculated using the following equation:

$$h_{cv} = \frac{q_{cv}}{(T_s - T_f)} \tag{23}$$

These coefficients are shown in Figure 6. The local convection heat transfer coefficients between the left and right surfaces and the air of the outer air gap are shown in Figure 6a and those of the inner air gap obtained by the CFD simulations are shown in Figure 6b.

It is noted that, in the upper section of the outer air gap, the local convective heat transfer coefficients between the channel's left surface and the air were negative. This does not make physical sense. In fact, we did not follow the basic definition of the convective heat transfer coefficient equation where the fluid temperature was that of a fluid sufficiently far from the surface, but we used the definition of the bulk air temperature. The convective heat flux relative to this surface was positive, while the temperature difference was negative.

Gloriant identified this phenomenon while investigating the thermal behavior of parietodynamic windows [35]. It is well explained when observing the local temperature profile in the air gap (Figure 7): the temperature gradient was negative at the left wall of the air gap, while the flux q_g was positive. However, since the temperature difference $(T_{sg} - T_m)$ was negative, we obtained a negative coefficient. Gloriant concluded that the temperature difference $(T_{sg} - T_m)$ under asymmetrical heating conditions is not representative of the direction of heat flow.

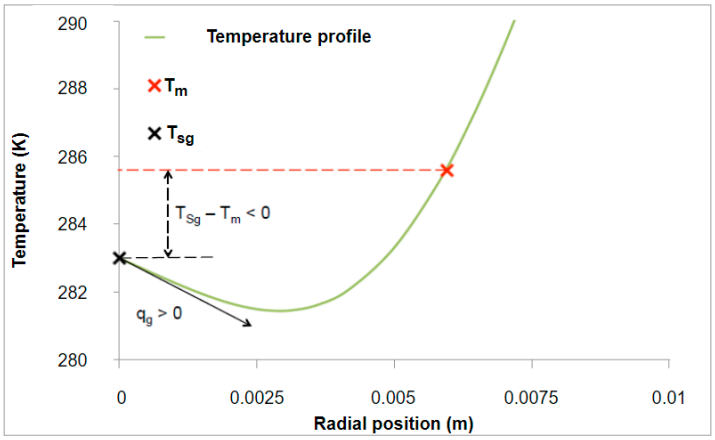

Figure 7. Temperature profile in the air gap [35]. Reprinted with permission from Ref. [35]. Copyright 2014 Gloriant, F.A.F. All rights reserved.

In fact, the air bulk temperature uses the temperature and velocity profiles cannot meaningfully be used to evaluate these coefficients. In the second air gap, extremely high values of local convective heat transfer coefficients were obtained between the left surface of the inner glazing and the air, where the air bulk temperature coincided with the surface temperature. For the above reasons, we chose to calculate the average convective heat transfer coefficients for the two air gaps.

Figure 8 shows the evolution of the heat transfer coefficients as a function of mass flow rate. For the outer air gap, as the mass flow rate increased, the convective heat transfer coefficient on the left (l) side decreased, while that on the right (r) side increased. For the second air gap, when the mass flow rate increased, the convective heat transfer coefficient towards the left side decreased, while for the right side it was almost stable. The same appearance of the curves was found as for the Paziaud window [35].

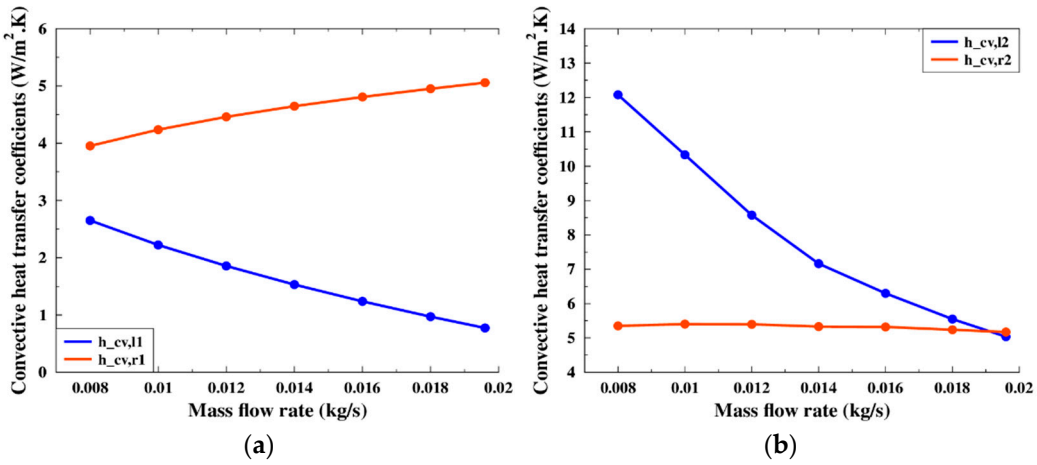

Figure 8. Convective heat transfer coefficients in the (**a**) outer gap and (**b**) inner gap.

It should be noted that similar results were obtained for the other simulations carried out with different imposed mass flow rates.

3.4.3. Effects of Airflow Rate

Figure 9 shows the temperature of the incoming air as a function of airflow when the outside air temperature is 0 °C, with an incident solar radiation of 300 W·m^{-2}. The heat convection between the surface cavities and the air was enhanced as the air mass flow rate increased, and the temperatures of the exterior surface of the massive wall and air cavity

surfaces were decreased. Hence, the outlet temperature of the air decreased. However, the heat gain, which included transmission losses, increased.

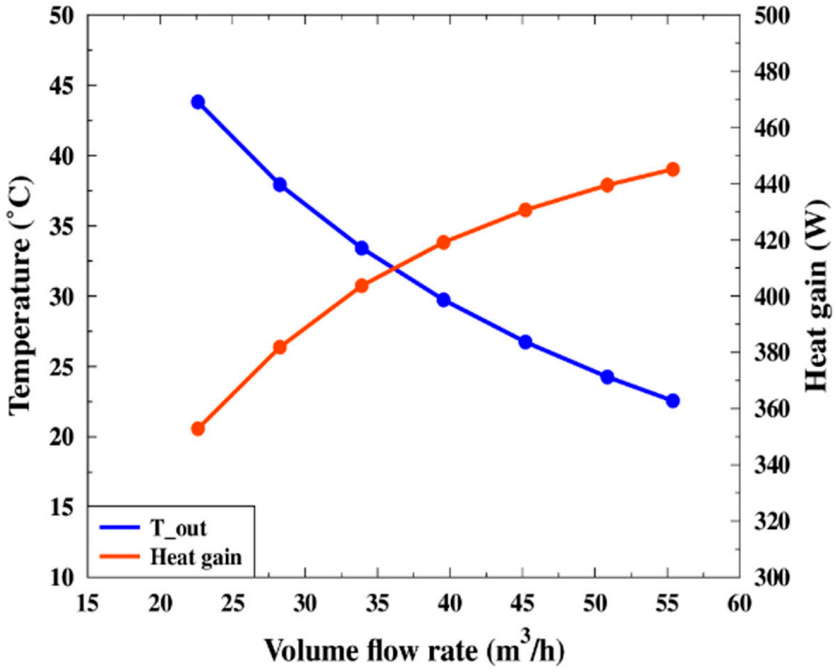

Figure 9. Variation in outlet temperature and heat gain with the imposed airflow rate.

Figure 10 shows the variation of the Reynolds number as a function of the imposed mass flow.

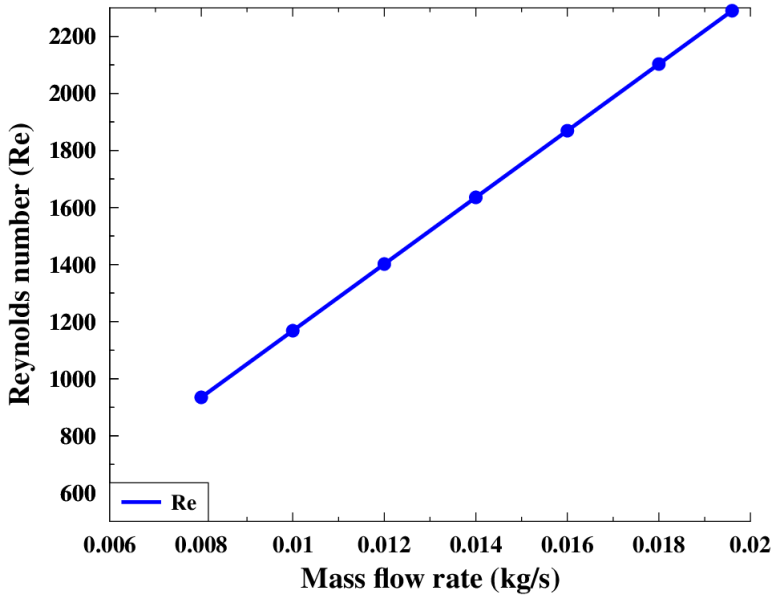

Figure 10. Variation in Reynolds number with pressure difference (Pa).

4. Formulation of the Model Adapted to Building Simulation

The overall model developed is one-dimensional. Figure 11 shows a representative diagram of the solar wall through an electrical analogy. The diagram shows the different surface nodes used and the different flows considered. On each node, the heat balance equation is solved and includes heat transfer due to convection, conduction, and radiation.

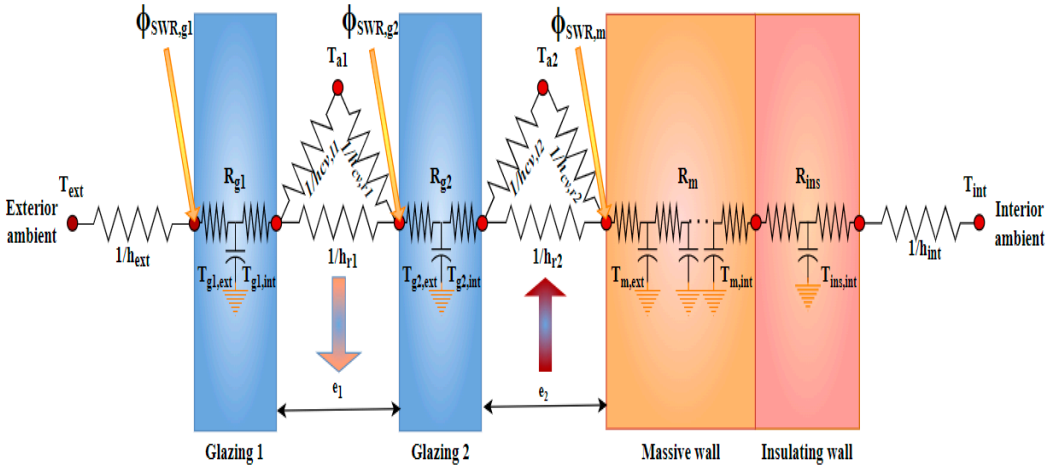

Figure 11. Schematic of the thermal resistance network for the VSW.

- Heat transfer with the surrounding environment

$$h_{ext} = 20\ \mathrm{W{\cdot}m^{-2}{\cdot}K^{-1}} \text{ and } h_{int} = 3.6\ \mathrm{W{\cdot}m^{-2}{\cdot}K^{-1}} \tag{24}$$

- Conduction in each solid layer

Conduction in the solid parts (finite difference method) is given by the one-dimensional conduction equation (Fourier's law) [8]:

$$\frac{\partial T(x,t)}{\partial t} = a\frac{\partial^2 T(x,t)}{\partial x^2} \tag{25}$$

The thermal diffusivity $\mathrm{m^2{\cdot}s^{-1}}$ is calculated by:

$$a = \frac{\lambda}{\rho C_p} \tag{26}$$

The numerical method used to solve the differential transient thermal conduction equation is the finite difference method. The massive wall is subdivided into 10 sections of equal thickness Δx.

$$\frac{T_i^{n+1} - T_i^n}{\Delta t} = a\left(\frac{T_{i+1}^n - 2T_i^n + T_{i-1}^n}{(\Delta x)^2}\right) \tag{27}$$

- Long Wave Radiation Heat transfer within the two air gaps

The heat transfer coefficients of the long-wave radiation between the two surfaces of the outer air gap as well as between the two surfaces of the inner air gap are given by Equations (28) and (29), respectively [3].

$$h_{r1} = \frac{\sigma(T_{g1,int} + T_{g2,ext})(T_{g1,int}^2 + T_{g2,ext}^2)}{\frac{1}{\varepsilon_{g1,int}} + \frac{1}{\varepsilon_{g2,ext}} - 1} \tag{28}$$

$$h_{r2} = \frac{\sigma(T_{g2,int} + T_{m,ext})(T_{g2,int}^2 + T_{m,ext}^2)}{\frac{1}{\varepsilon_{g2,int}} + \frac{1}{\varepsilon_{m,ext}} - 1} \tag{29}$$

- Convective heat transfers in the cavities

The energy transferred to the air by convection is equal to the change in enthalpy of the air in the control volume. The convective heat transfer for a differential control volume in the air cavity is shown in Figure 12.

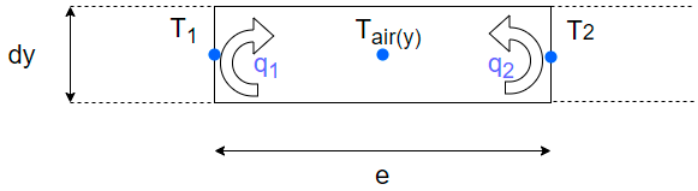

Figure 12. Schematic of convective heat transfer for a differential control volume of the air cavity.

If we consider a uniform surface temperature on both sides for steady flow, we obtain a first-order differential equation with a second member that represents the local heat balance of the air.

$$\dot{m}C_p dT_{air}(y) = (q_1 + q_2)wdy \tag{30}$$

where q_1 and q_2 are the heat exchange by convection of the first and second wall, respectively.

$$\dot{m}C_p dT_{air}(y) = h_1(T_1 - T_{air}(y))wdy + h_2(T_2 - T_{air}(y))wdy \tag{31}$$

The solution of this differential equation is as follows:

$$T_{a1}(y) = (T_{inlet,1} - \frac{h_{cv,l1}T_{g1,int} + h_{cv,r1}T_{g2,ext}}{h_{cv,l1} + h_{cv,r1}})e^{-\frac{w(h_{cv,l1}+h_{cv,r1})}{\dot{m}C_p}y} + \frac{h_{cv,l1}T_{g1,int} + h_{cv,r1}T_{g2,ext}}{h_{cv,l1} + h_{cv,r1}} \tag{32}$$

$$T_{a2}(y) = (T_{inlet,2} - \frac{h_{cv,l2}T_{g2,int} + h_{cv,r2}T_{m,ext}}{h_{cv,l2} + h_{cv,r2}})e^{-\frac{w(h_{cv,l2}+h_{cv,r2})}{\dot{m}C_p}y} + \frac{h_{cv,l2}T_{g2,int} + h_{cv,r2}T_{m,ext}}{h_{cv,l2} + h_{cv,r2}} \tag{33}$$

The convective heat transfer coefficients between the surfaces of the VSW cavities and the air must be predetermined or determined using empirical equations. Hence, we developed two simplified models, both adapted to building simulation, that differ in the method of determining the convective heat transfer coefficients.

SM1: Using CFD results;

SM2: Using the analytical relations of Shah and London [36] that correspond to forced convection in a vertical channel with asymmetrical heating.

$$N_{u11} = \frac{140}{26 - 9\frac{q_2}{q_1}} \; and \; N_{u12} = \frac{140}{26 - 9\frac{q_1}{q_2}} \tag{34}$$

Energy Balance Equations

Equations (35)–(40) correspond, respectively, to energy balances at the external and internal surfaces of the glazings, the exterior surface of the massive wall, and the interior surface of the insulation wall.

$$\phi_{SWR,\,g1} + Ah_{r,gnd}(T_{gnd} - T_{g1,ext}) + Ah_{r,sky}(T_{sky} - T_{g1,ext}) + Ah_{cv,ext}(T_{sky} - T_{g1,ext}) = -\lambda A\frac{dT}{dx})_{x=0} \tag{35}$$

$$Ah_{r1}(T_{g1,int} - T_{g2,ext}) + Ah_{cv,l1}(T_{g1,int} - T_{a1}) = -\lambda A\frac{dT}{dx})_{x=4\text{ mm}} \tag{36}$$

$$\phi_{SWR,\,g2} + Ah_{r1}(T_{g1,int} - T_{g2,ext}) + Ah_{cv,r1}(T_{a1} - T_{g2,ext}) = -\lambda A\frac{dT}{dx})_{x=4\text{ mm}} \tag{37}$$

$$Ah_{r2}(T_{g2,int} - T_{m,ext}) + Ah_{cv,l2}(T_{g2,int} - T_{a2}) = -\lambda A\frac{dT}{dx})_{x=23\text{ mm}} \tag{38}$$

$$\phi_{SWR,\,m} + Ah_{r2}(T_{g2,int} - T_{m,ext}) + Ah_{cv,r2}(T_{a2} - T_{m,ext}) = -\lambda A\frac{dT}{dx})_{x=38\text{ mm}} \tag{39}$$

$$Ah_{r,int}(T_{ins} - T_{int}) + Ah_{cv,int}(T_{ins} - T_{int}) = -\lambda A\frac{dT}{dx})_{x=258\text{ mm}} \tag{40}$$

- Implementation of the simplified model in Modelica library

Dymola is a modeling and simulation environment based on the open Modelica language. It is an object-oriented language using a multi-disciplinary system with acausal modeling. The benefit of this language is its richness in libraries that can meet the diversified needs of physicists. Dymola (version 2019, Dassault Systèmes) was chosen as the simulation environment to conduct the work of our study.

In choosing the most suitable library for the dynamic thermal simulation of our studied solar system, reference was made to the study conducted by Tittelein et al. In this study, a comparison of seven free Modelica libraries (Aixlib, Annex60, ATPlus, Buildings, BuildingSystem, BuildSysPro, IDEAS) was performed, mainly focusing on model functionality. The example of the integration of the parietodynamic window was presented. The model to be integrated and the hosting library must have the same connectors [37].

Our model consists, first, in preheating the new ventilation air; then, the model to be developed in Dymola must simulate the fluid flow during its passage through the solar system from the external environment to the internal environment (room). Therefore, the model must be integrated into a library that includes the connectors "fluidPort" and "heatPort"; this allows it to be connected to the building model. In addition, the modeler is always looking for a library with complete documentation that is always up to date. Hence, we chose the "library: buildings" [38]. The simplified developed model is shown in Figure 13.

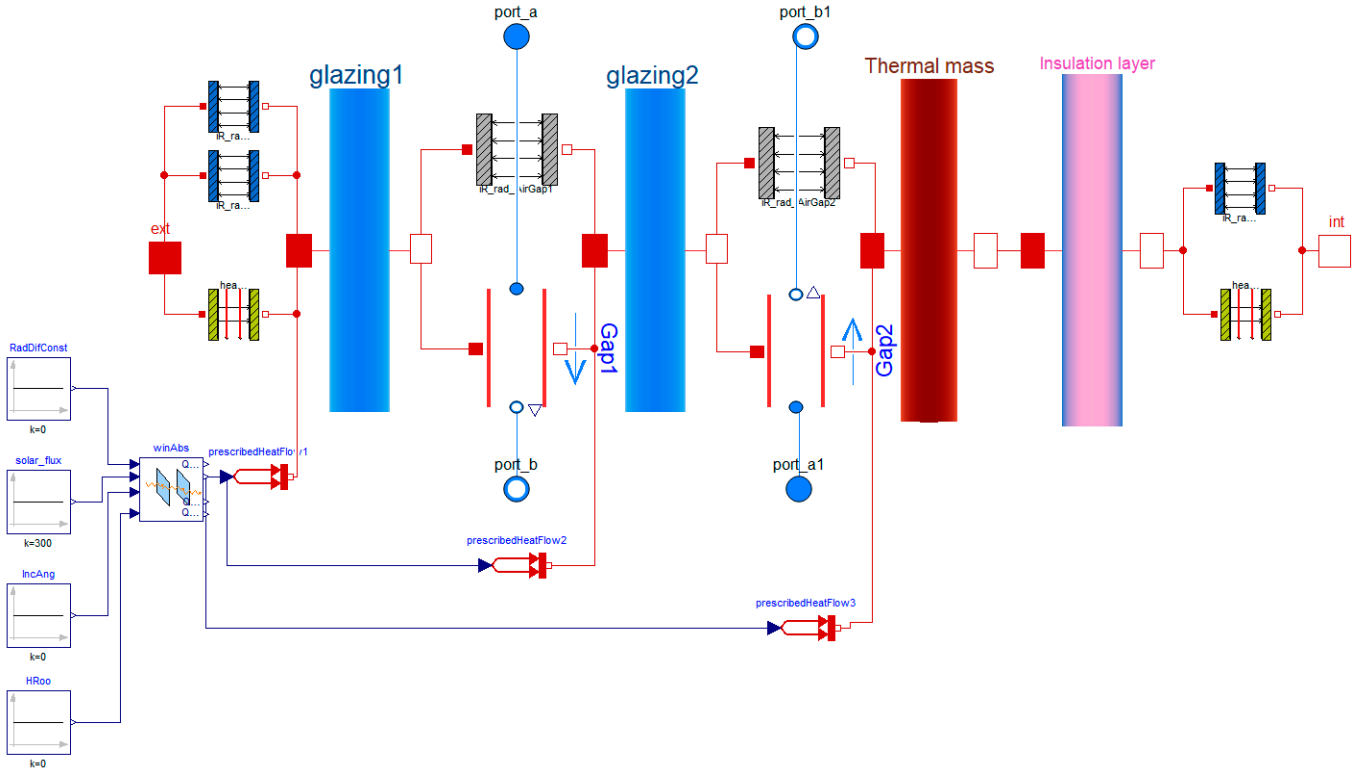

Figure 13. Modelica model for the VSW.

5. Results and Discussions

- Thermal Performance of VSW with airflow rate

The outlet air temperature values from the CFD model and the two simplified models are provided by Figure 14. They correspond to the values calculated at the exit of the VSW. The figure also represents the heat gain obtained with the VSW for the three cases. The outlet air temperature appears to evolve according to a decreasing exponential.

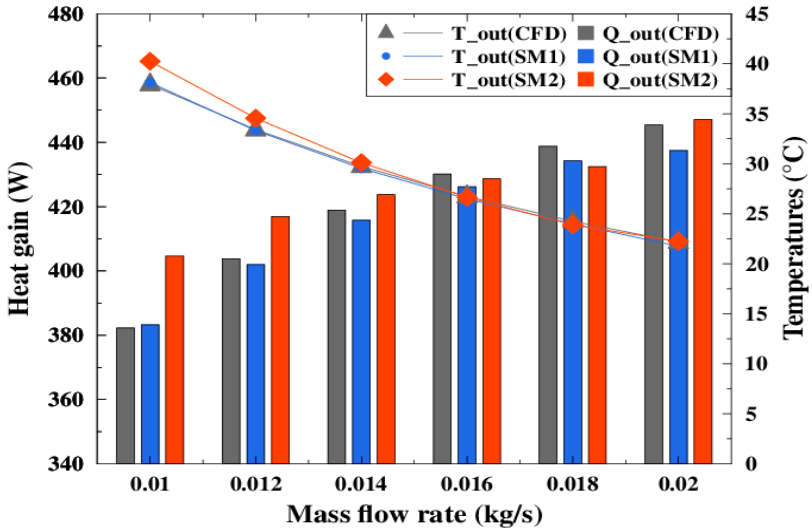

Figure 14. Variation in the temperature and heat gain of the air at the outlet with mass flow rate.

To evaluate the results, the relative error was used as an indicator. The RE between CFD and the analytical results was calculated by:

$$RE = \left| \frac{X_{CFD} - X_{SM}}{X_{CFD}} \right|$$

The outlet air temperature values predicted by the first simplified model were extremely close to those obtained by the CFD study ($\Delta T < 0.4$ °C). The difference in heat gain values between the two models was less than 1%.

The results from the CFD model are in good agreement with those from the simplified models. Moreover, SM1 is more accurate than SM2. However, a single CFD simulation can provide only one result under a given condition. It would thus be necessary to perform a CFD simulation each time a wall parameter is modified and recalculate the corresponding convective heat transfer coefficients. Therefore, it is more convenient to work with SM2. In the next sections, the SM2 is tested under different solar radiation conditions.

- Thermal Performance of VSW with Solar Irradiation

Figure 15 presents the simulation results for the heat balance as a function of incident solar radiation for both systems. Good agreement was found between the CFD model and SM2. The relative error for heat gain between the two models was less than 10%.

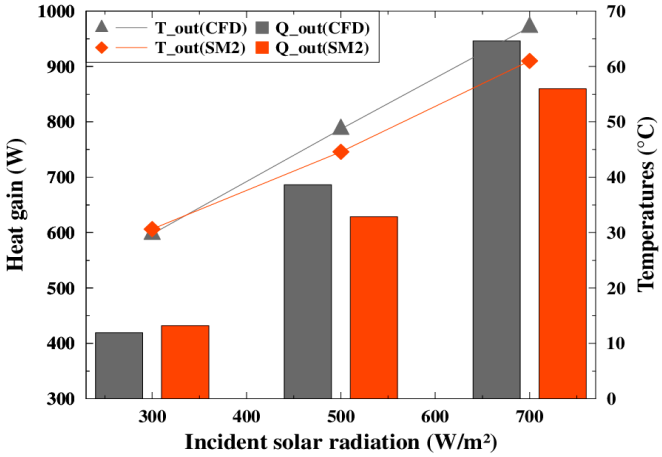

Figure 15. Variation in the temperature and heat gain of the air at the outlet with incident solar radiation.

- No solar radiation

The comparison indicates that the simulated results agree well with the CFD results, and their variation tendencies are consistent, which means that the simulation model has acceptable and reasonable accuracy for evaluating the thermal performance and calculating the annual energy consumption of the VSW. The model is a little less accurate when there is no solar radiation (see Figure 16): the relative error increased from 15% to 25% as the air mass flow rate increased from 0.01 kg/s to 0.018 kg/s, but this remains acceptable.

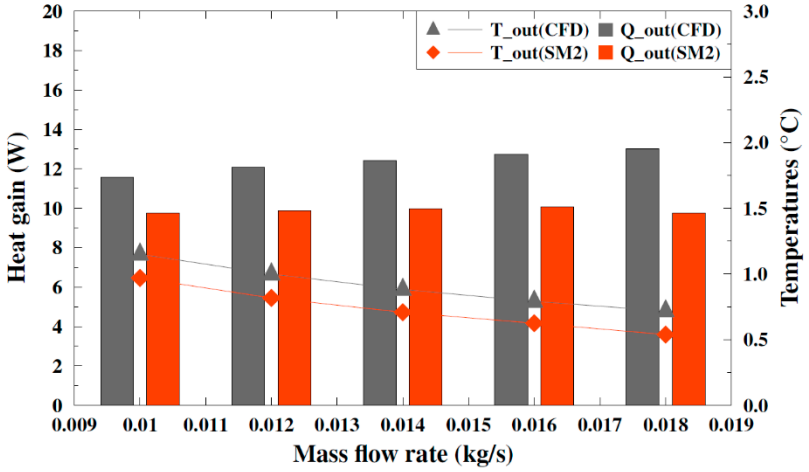

Figure 16. Variation in the temperature and heat gain of the air at the outlet with mass flow rate (no solar radiation).

- Contribution of each air gap to the heat gain

The contribution of each of the two air gaps to the preheating of the fresh ventilation air is given in Figure 17. The results indicate that the heat flux gained by the air occurred mainly in the second air gap, and as the airflow rate increased, this effect became more apparent. Approximately, the first air gap accounted for only one-third of the recovered heat flow.

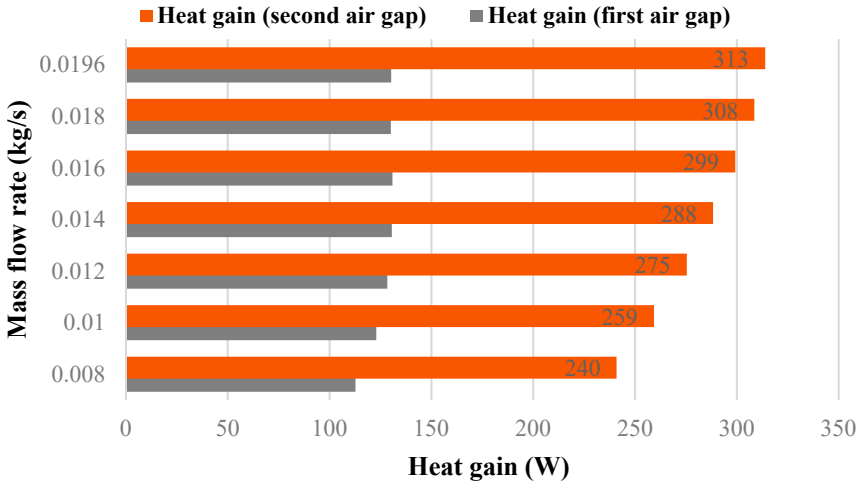

Figure 17. Contribution of air gaps in air preheating.

- Performance of the VSW

The thermal efficiency of the VSW is calculated as the ratio of the useful heat gain to the global solar power received by the solar façade (see Equation (2)). This is valid because it is considered that the wall is insulated and therefore that the flow recovered through the insulation is almost zero.

As mentioned before, the simulations were carried out under steady-state conditions.

At this stage of the investigation, numerical modeling showed a promising potential for the ventilated solar wall studied. The thermal efficiency of the wall increased with a mass flow rate between 55% and 70% (Figure 18). It was very effective compared to other kinds of solar walls (see Table 1).

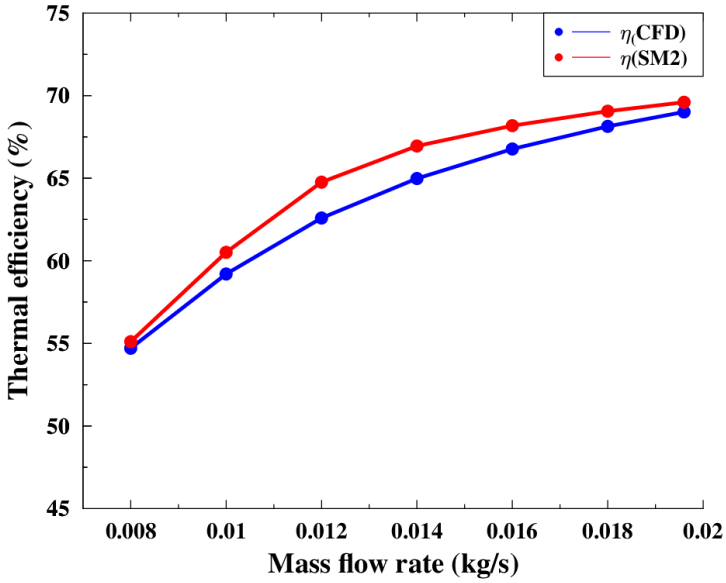

Figure 18. Variation in the thermal efficiency of the VSW with the airflow rate.

At this level, this modeling demonstrated that VSW can provide much energy to a building. System performance may be accurately assessed by evaluating its thermal efficiency throughout the heating season when the model is integrated into a building energy simulation.

6. Conclusions

In this paper, a new concept of a ventilated solar façade system was presented that can be integrated into a building's envelope. Detailed analysis of heat transfers and fluid flow inside the ventilated cavities was performed with CFD simulations under forced convection. Particular attention was given to the calculation of the convective heat transfer coefficients in the two ventilated air cavities.

We proposed two simplified models adapted to BES that aim to simplify the heat transfer calculation involved in the VSW. In this model, two methods for calculating the convective heat transfer coefficients were proposed for the heat transfer between the air gap surfaces and the flowing air. The first model requires a preliminary CFD calculation, in contrast to the second model, which uses analytical relations. We found the first model to be more accurate than the second, but since it requires performing a new simulation each time a variable is changed, we found the second model to be satisfactory for our application.

The results show that this type of supply-air façade can provide preheated fresh air to buildings. The thermal performance of VSW increased with a mass flow rate between 55 and 70%. It is essential to note that all the simulations were performed in a steady state.

Although at this preliminary stage of analysis VSW may provide a sustainable model for future applications in building façades, further research is recommended, including incorporating the model into a BES code and evaluating its ability to restore the stored thermal energy when this is needed and consequently its potential to reduce energy consumption for the heating season. Experimental validation of the model is also recommended.

Author Contributions: Conceptualization, R.A.I., P.T., L.Z., S.L. and F.H.C.; methodology R.A.I., P.T., L.Z., S.L. and F.H.C.; investigation, R.A.I., P.T., L.Z., S.L. and F.H.C.; data curation, R.A.I., P.T., L.Z., S.L. and F.H.C.; writing—original draft R.A.I.; writing—editing R.A.I., P.T., L.Z., S.L. and F.H.C. All authors have read and agreed to the published version of the manuscript.

Funding: This research received no external funding.

Conflicts of Interest: The authors declare that they have no known competing financial interests or personal relationships that could have appeared to influence the work reported in this paper.

Nomenclature

A	Ventilated solar wall area (m^2)
BES	Building energy simulation
CFD	Computational fluid dynamics
C_p	Specific heat capacity ($J \cdot kg^{-1} \cdot K^{-1}$)
D_h	Hydraulic diameter (m)
DSF	Double-skin façade
h_{cv}	Convection heat transfer coefficient ($W \cdot m^{-2} \cdot K^{-1}$)
h_r	Radiation heat transfer coefficient ($W \cdot m^{-2} \cdot K^{-1}$)
H	VSW height (m)
I	Incident solar radiation ($W \cdot m^{-2}$)
LWR	Longwave radiation
l	Left
Nu	Nusselt number
r	Right
R	Thermal resistance ($m^2 \cdot K \cdot W^{-1}$)
SWR	Short wave radiation
Re	Reynolds number
Ri	Richardson number
T	Temperature (°C)
VSW	Ventilated solar wall
w	VSW width (m)
Greek letters	
α	Solar absorptivity
ε	Emissivity
λ	Thermal conductivity ($W \cdot m^{-1} \cdot K^{-1}$)
μ	Dynamic viscosity ($kg \cdot m^{-1} \cdot s^{-1}$)
ν	Kinematic viscosity ($m^2 \cdot s^{-1}$)
ξ	Solar absorption factor
ρ	Density ($kg \cdot m^{-3}$)
σ	Stefan–Boltzmann constant (5.67×10^{-8} $W \cdot m^{-2} \cdot K^{-4}$)
Subscript	
cond	Conduction
cv	Convection
ext	External ambient
g	Glass
gnd	Ground
in	Inlet
ins	Insulation
int	Internal ambient
m	Massive wall
1,2	Glass identification index

References

1. Khedari, J.; Boonsri, B.; Hirunlabh, J. Ventilation impact of a solar chimney on indoor temperature fluctuation and air change in a school building. *Energy Build.* **2000**, *32*, 89–93. [CrossRef]
2. Lee, K.H.; Strand, R.K. Enhancement of natural ventilation in buildings using a thermal chimney. *Energy Build.* **2009**, *41*, 615–621. [CrossRef]

3. Zhang, C.; Gang, W.; Wang, J.; Xu, X.; Du, Q. Numerical and experimental study on the thermal performance improvement of a triple glazed window by utilizing low-grade exhaust air. *Energy* **2018**, *167*, 1132–1143. [CrossRef]
4. Carlos, J.; Corvacho, H.; Silva, P.; Castro-Gomes, J. Real climate experimental study of two double window systems with preheating of ventilation air. *Energy Build.* **2010**, *42*, 928–934. [CrossRef]
5. Gloriant, F.; Tittelein, P.; Joulin, A.; Lassue, S. Modeling a triple-glazed supply-air window. *Build. Environ.* **2015**, *84*, 1–9. [CrossRef]
6. Michaux, G.; Greffet, R.; Salagnac, P.; Ridoret, J.-B. Modelling of an airflow window and numerical investigation of its thermal performances by comparison to conventional double and triple-glazed windows. *Appl. Energy* **2019**, *242*, 27–45. [CrossRef]
7. Kaboré, M.; Michaux, G.; le Dréau, J.; Salagnac, P.; Greffet, R. Parametric study of the thermal performance of a sin-gle-family house equipped with an airflow window integrating a heated glazing. In Proceedings of the Building Simulation 2019, 16th IBPSA International Conference, Roma, Italy, 2–4 September 2019.
8. Shen, J.; Lassue, S.; Zalewski, L.; Huang, D. Numerical study on thermal behavior of classical or composite Trombe solar walls. *Energy Build.* **2007**, *39*, 962–974. [CrossRef]
9. Leang, E.; Tittelein, P.; Zalewski, L.; Lassue, S. Numerical study of a composite Trombe solar wall integrating microen-capsulated PCM. *Energy Procedia* **2017**, *122*, 1009–1014. [CrossRef]
10. Simões, N.; Manaia, M.; Simões, I. Energy performance of solar and Trombe walls in Mediterranean climates. *Energy* **2021**, *234*, 121197. [CrossRef]
11. Khosravi, S.N.; Mahdavi, A. A CFD-Based Parametric Thermal Performance Analysis of Supply Air Ventilated Windows. *Energies* **2021**, *14*, 2420. [CrossRef]
12. Wei, J.; Zhao, J.; Chen, Q. Energy performance of a dual airflow window under different climates. *Energy Build.* **2010**, *42*, 111–122. [CrossRef]
13. Fantucci, S.; Serra, V.; Perino, M. Dynamic Insulation Systems: Experimental Analysis on a Parietodynamic Wall. *Energy Procedia* **2015**, *78*, 549–554. [CrossRef]
14. Saelens, D.; Roels, S.; Hens, H. Strategies to improve the energy performance of multiple-skin facades. *Build. Environ.* **2008**, *43*, 638–650. [CrossRef]
15. De Gracia, A.; Navarro, L.; Castell, A.; Ruiz-Pardo, Á.; Alvárez, S.; Cabeza, L.F. Experimental study of a ventilated facade with PCM during winter period. *Energy Build.* **2013**, *58*, 324–332. [CrossRef]
16. Wang, Y.; Chen, Y.; Lia, C. Energy performance and applicability of naturally ventilated double skin façade with venetian blinds in Yangtze river area. *Sustain. Cities Soc.* **2020**, *61*, 102348. [CrossRef]
17. Faggembauu, D.; Costa, M.; Soria, M.; Oliva, A. Numerical analysis of the thermal behaviour of glazed ventilated facades in Mediterranean climates. Part II: Applications and analysis of results. *Solar Energy* **2003**, *75*, 229–239. [CrossRef]
18. Fallahi, A.; Haghighat, F.; Elsadi, H. Energy performance assessment of double-skin façade with thermal mass. *Energy Build.* **2010**, *42*, 1499–1509. [CrossRef]
19. Richman, R.; Pressnail, K. Quantifying and predicting performance of the solar dynamic buffer zone (SDBZ) curtain wall through experimentation and numerical modeling. *Energy Build.* **2010**, *42*, 522–533. [CrossRef]
20. Leang, E.; Tittelein, P.; Zalewski, L.; Lassue, S. Impact of a Composite Trombe Wall Incorporating Phase Change Materials on the Thermal Behavior of an Individual House with Low Energy Consumption. *Energies* **2020**, *13*, 4872. [CrossRef]
21. Michaux, G.; Greffet, R.; Salagnac, P.; Ridoret, J.-B. *Etude Numérique des Performances Thermiques d'une Maison Individuelle Equipée de Fenêtres Pariétodynamiques*; Société Française de Thermique: Marseille, France, 2017.
22. Hong, X.; He, W.; Hu, Z.; Wang, C.; Ji, J. Three-dimensional simulation on the thermal performance of a novel Trombe wall with venetian blind structure. *Energy Build.* **2014**, *89*, 32–38. [CrossRef]
23. Bojić, M.; Johannes, K.; Kuznik, F. Optimizing energy and environmental performance of passive Trombe wall. *Energy Build.* **2014**, *70*, 279–286. [CrossRef]
24. Jaber, S.; Ajib, S. Optimum design of Trombe wall system in mediterranean region. *Sol. Energy* **2011**, *85*, 1891–1898. [CrossRef]
25. Richman, R.; Pressnail, K. A more sustainable curtain wall system: Analytical modeling of the solar dynamic buffer zone (SDBZ) curtain wall. *Build. Environ.* **2009**, *44*, 1–10. [CrossRef]
26. Jankovic, A.; Goia, F. Impact of double skin facade constructional features on heat transfer and fluid dynamic behaviour. *Build. Environ.* **2021**, *196*, 107796. [CrossRef]
27. Hult, E.L.; Iaccarino, G.; Fischer, M. Using CFD Simulations to Improve the Modeling of Window Discharge Coefficients. *Proc. SimBuild* **2012**, *5*, 322–328.
28. Bhamjee, M.; Nurick, A.; Madyira, D. An experimentally validated mathematical and CFD model of a supply air window: Forced and natural flow. *Energy Build.* **2012**, *57*, 289–301. [CrossRef]
29. WINDOW 7 Software, v7.7.1.0, Lawrence Berkeley National Laboratory, University of California, USA. Available online: https://windows.lbl.gov/software/window (accessed on 11 March 2022).
30. Lucchino, E.C.; Goia, F.; Lobaccaro, G.; Chaudhary, G. Modelling of double skin facades in whole-building energy simulation tools: A review of current practices and possibilities for future developments. *Build. Simul.* **2019**, *12*, 3–27. [CrossRef]
31. ISO-15099. Thermal Performance of Windows, Doors and Shading Devices. Available online: https://www.iso.org/standard/26425.html (accessed on 11 March 2022).

32. Padet, J.; Cotta, R.M.; Mladin, E.C.; Padet, C. Mixed thermal convection: Fundamental issues and analysis of the planar case. *An. Acad. Bras. Ciênc.* **2015**, *87*, 1865–1885. [CrossRef]
33. Cheng, C.-H.; Kou, H.-S.; Huang, W.-H. Flow reversal and heat transfer of fully developed mixed convection in vertical channels. *J. Thermophys. Heat Transf.* **1990**, *4*, 375–383. [CrossRef]
34. Nield, D. Forced convection in a parallel plate channel with asymmetric heating. *Int. J. Heat Mass Transf.* **2004**, *47*, 5609–5612. [CrossRef]
35. Gloriant, F.A.F. Caractérisation et Modélisation d'une Fenêtre Pariétodynamique à Trois Vitrages, Université d'Artois, France. 2014. Available online: http://www.theses.fr/2014ARTO0205 (accessed on 15 March 2022).
36. Shah, R.; London, A. *Laminar Flow Forced Convection in Ducts: A Source Book for Compact Heat Exchanger Analytical Data*; Academic Press: New York, NY, USA, 1978.
37. Tittelein, P.; Leang, E.; Zalewski, L.; Lassue, S. Comparaison des bibliothèques libres de Modelica pour la simulation thermique dynamique du bâtiment. In Proceedings of the Conférence IBPSA, Marne-la-Vallée, France, 15 May 2016.
38. Wetter, M.; Zuo, W.; Nouidui, T.S.; Pang, X. Modelica Buildings library. *J. Build. Perform. Simul.* **2014**, *7*, 253–270. [CrossRef]